Facile and Controllable Synthesis of CuS@Ni-Co Layered Double Hydroxide Nanocages for Hybrid Supercapacitors

Zhe Sheng, Xiongchao Lin,* Yiting Zhao, Lei Huang, Hongfeng Gao, Hao Wei, Caihong Wang, Deping Xu, and Yonggang Wang

ACCESS | Metrics & More | Article Recommendations | Supporting Information

ABSTRACT: The synthesis of battery-type electrode materials with hollow nanostructures for high-performance hybrid super-capacitors (HSCs) remains challenging. In this study, hollow CuS@Ni-Co layered double hydroxide (CuS-LDH) composites with distinguished compositions and structures are successfully synthesized by co-precipitation and the subsequent etching/ion-exchange reaction. CuS-LDH-10 with uniformly dispersed CuS prepared with the addition of 10 mg of CuS shows a unique hollow polyhedral structure constituted by loose nanosphere units, and these nanospheres are composed of interlaced fine nanosheets. The composite prepared with 30 mg of CuS addition (CuS-LDH-30) is composed of a hollow cubic morphology with vertically aligned nanosheets on the CuS shell. The CuS-LDH-10 and CuS-LDH-30 electrodes exhibit high specific capacity (765.1 and 659.6 C g^{-1} at 1 A g^{-1}, respectively) and superior cycling performance. Additionally, the fabricated HSC delivers a prominent energy density of 52.7 Wh kg^{-1} at 804.5 W kg^{-1} and superior cycling performance of 87.9% capacity retention after 5000 cycles. Such work offers a practical and effortless route for synthesizing unique metal sulfide/hydroxide composite electrode materials with hollow structures for high-performance HSCs.
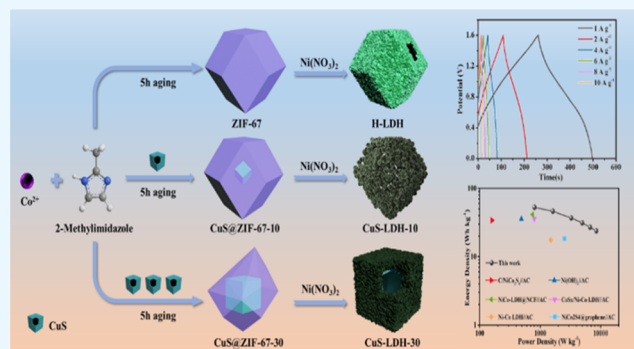
1. INTRODUCTION

Today, the energy crisis and environmental sustainability have forced us to develop more advanced energy systems.[1−4] Among the emerging energy storage devices, supercapacitors (SCs) have drawn significant attention because of their excellent cycling stability, quick charge−discharge capability, and ultrahigh power density.[5−7] However, the insufficient energy density dramatically hinders their further commercial application.[8,9] To enhance the energy densities, hybrid supercapacitors (HSCs) have become one of the promising development approaches by combining the excellent energy density of battery-type faradaic electrodes with a carbon negative electrode.[10,11] The intrinsic properties of the battery-type materials are regarded as the vital factor in achieving high-performance HSCs.[12−15]

Transition metal compounds[16−19] are typical positive electrode materials with superior electrochemical performance. Among them, layered double hydroxides (LDHs) are commonly used as electrode materials, benefitting from their numerous redox states and high tunability of multivalent metal cations, as well as unique two-dimensional (2D) lamellar structures.[20−22] Nevertheless, LDHs are often plagued by their deficient conductivity, unacceptable structural stability, and strong stacking propensity.[23−25] Hollow nanostructures with well-defined interior voids are of great interest because of their

structural merits of shortened diffusion paths for charge transport and large surface permeability.[26,27] Accordingly, the design of LDH materials with hollow nanostructures is a promising approach to improving their electrochemical performance; however, it is still a huge challenge to create hollow structures with desired electrochemical performance. Zeolitic imidazolate frameworks (ZIFs) are comprised of metal ions and organic ligands.[28,29] ZIFs have tunable structures and can be employed as both metal precursors and sacrificial templates to fabricate well-defined hollow structures.[30−32] Chen et al.[33] successfully prepared hollow NiCo-LDH nanocage materials with excellent electrochemical properties using ZIF-67 as a precursor. Generally, MOF-derived hollow LDH materials have insufficient structural stability and conductivity, resulting in the attenuation of electrochemical properties.[20,34] It is considered that transition metal sulfides (TMSs) with lower energy band gap and higher electrical conductivity can combine with LDHs to effectively meliorate

Scheme 1. Schematic Illustration of the Preparation of Hollow H-LDH and CuS-LDH Nanocages
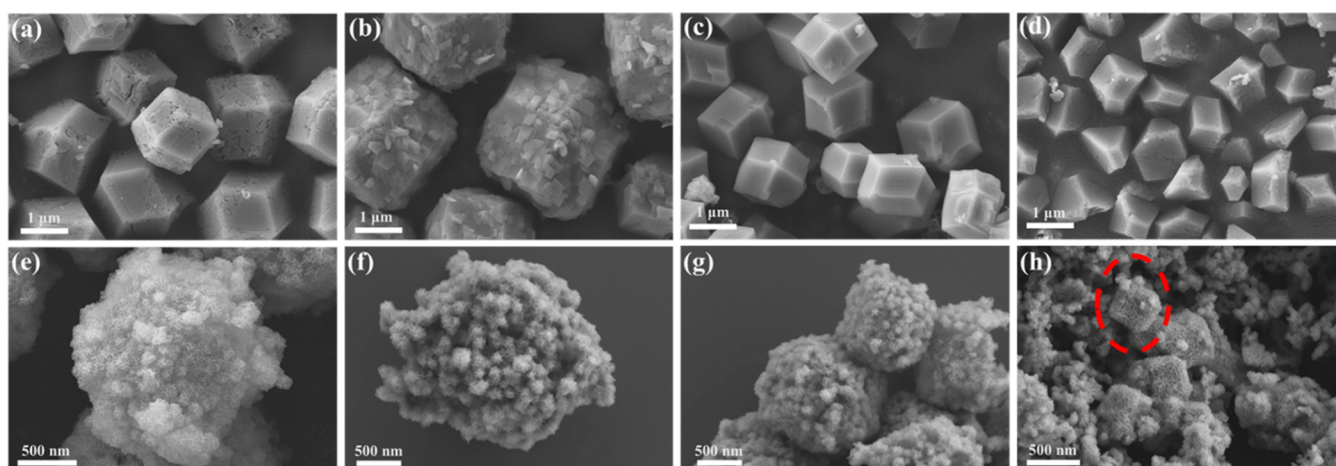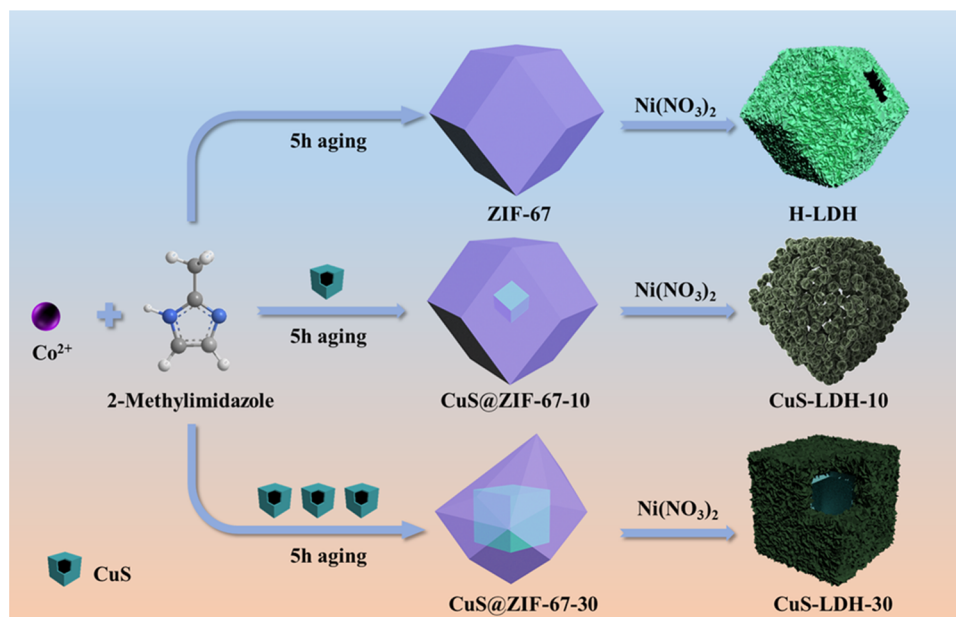

Figure 1. SEM images of (a) ZIF-67, (b) CuS@ZIF-67-10, (c) CuS@ZIF-67-20, (d) CuS@ZIF-67-30, (e) H-LDH, (f) CuS-LDH-10, (g) CuS-LDH-20, and (h) CuS-LDH-30.

their electrochemical performance.[35−38] Among the various metal sulfides, CuS possessing excellent metal-like conductivity, complex valence states, and controllable structures has attracted considerable attention.[39,40] Moreover, CuS can be prepared with diverse structures, such as nanoplates,[41] nano/microflowers,[42,43] nanocages,[44] and nanospheres,[39] for application in supercapacitors.

Herein, a feasible and effective route for synthesizing novel CuS@Ni-Co layered double hydroxide (CuS-LDH) composite materials with hollow structures is proposed. The key processes involve the synthesis of CuS@ZIF-67s by the growth reaction of ZIF-67 with different amounts of CuS and sequential transformation of CuS@ZIF-67s into CuS-LDHs by reaction with $Ni(NO_3)_2 \cdot 6H_2O$. The CuS-LDHs possess various morphologies and structures with different amounts of CuS addition. CuS-LDH-10 with uniformly dispersed CuS shows a unique hollow polyhedral structure constituted by loose nanosphere units, and these nanosphere units are composed of interlaced fine nanosheets, while the vertically aligned NiCo-LDH nanosheets of CuS-LDH-30 are

grown on the surface of the CuS shells to create the hollow cubic morphology. Significantly, the CuS-LDH-10 and CuS-LDH-30 electrodes exhibit high specific capacity (765.1 and 659.6 C g^{-1} at 1 A g^{-1}, respectively) and superior cycling performance. Additionally, the fabricated HSC device (CuS-LDH-10//active carbon) exhibits a maximum energy density of 52.7 Wh kg^{-1} at 804.5 W kg^{-1} and superior cycling stability (87.9% capacity retention after 5000 cycles).

2. RESULTS AND DISCUSSION

2.1. Characterization of Morphology and Structure. The synthesis procedure of CuS-LDH composite materials is illustrated in Scheme 1. The scanning electron microscopy (SEM) images (Figures S1a and S2a) demonstrate that the prepared Cu_2O and CuS have cubic shapes and hollow cubic morphologies, respectively. The X-ray diffraction (XRD) patterns of prepared Cu_2O (Figure S1b) and CuS (Figure S2b) can be readily assigned to the reported pure Cu_2O (JCPDS 78-2076)[45] and CuS (JCPDS 06-0464), respec-
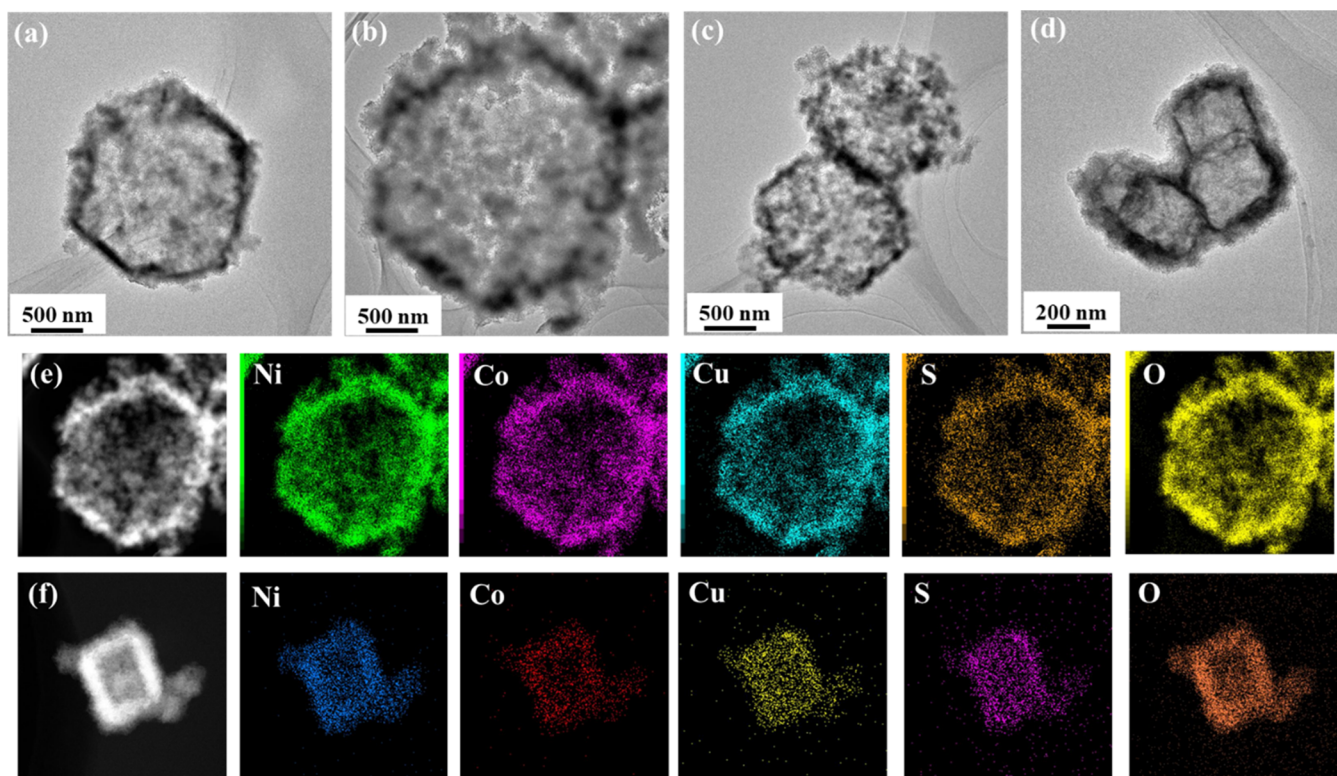
Figure 2. TEM images of (a) H-LDH, (b) CuS-LDH-10, (c) CuS-LDH-20, and (d) CuS-LDH-30 and EDS mappings of (e) CuS-LDH-10 and (f) CuS-LDH-30.

tively.[46−48] These results demonstrate the successful synthesis of CuS nanoboxes.

The structures and morphologies of the as-prepared ZIF-67, CuS@ZIF-67s, H-LDH, and CuS-LDH materials were detected using SEM, as displayed in Figure 1. The structures of CuS@ZIF-67s prepared with different amounts of CuS demonstrate significant differences from that of ZIF-67 because of the nucleation effect of CuS, and the CuS nanoboxes are wrapped in CuS@ZIF-67s. ZIF-67 (Figure 1a) possesses a typical rhombic dodecahedron structure with some cracks and pores on the surface, and its average particle size is approximately 1.5 μm. CuS@ZIF-67-10, CuS@ZIF-67-20, and CuS@ZIF-67-30 (Figure 1b−d) present distorted rhombic dodecahedron structures, and their average particle sizes are ca. 2.7 μm, 1.2 μm, and 750 nm, respectively. CuS@ZIF-67-10 shows a rough surface with some flake particles, which might be caused by the adsorption of incompletely formed ZIF-67. CuS@ZIF-67-10 has a much larger particle size than that of ZIF-67, while the particle size of CuS@ZIF-67-30 is slightly larger than the size of CuS (450 nm) due to the addition of more CuS nuclei during the growth process of ZIF-67. Hollow H-LDH and CuS-LDH nanocages were synthesized by adding $Ni(NO_3)_2 \cdot 6H_2O$ to react with ZIF-67 and CuS@ZIF-67s, respectively. According to the SEM images (Figure 1e), the H-LDH nanocages inherit the polyhedron structure of ZIF-67, and their surfaces are constituted by the vertically arranged nanosheets. CuS-LDH-10 (Figure 1f) is composed of abundant uniform nanospheres, which are fabricated by the reasonable stacking of NiCo-LDH nanosheets. Moreover, CuS-LDH-20 (Figure 1g) demonstrates a distorted polyhedron structure and is also composed of nanospheres similar to CuS-LDH-10, but the nanospheres are more compact. Whereas the structure of CuS-LDH-30 is

closer to CuS nanoboxes, and the vertically arranged nanosheets grow uniformly on their cubic shell; besides, some damaged structures can also be found in Figure 1h.

The H-LDH and CuS-LDH samples prepared with different amounts of CuS were further analyzed using transmission electron microscopy (TEM) to determine the inherent properties and formation mechanism. The formation mechanism of the ultrathin nanosheet NiCo-LDH is tentatively proposed. Primarily, the protons generated from the hydrolysis of $Ni(NO_3)_2$ etch ZIF-67. Subsequently, the released Co^{2+} is partially oxidized by dissolved oxygen and NO_3^-. Eventually, the formed Co^{2+}/Co^{3+} co-precipitates with Ni^{2+} ions to obtain NiCo-LDH nanosheets.[49] The TEM images (Figure 2a−d) further confirm the hollow structures with a homogeneous nanosheet array of the as-prepared samples after reacting with $Ni(NO_3)_2 \cdot 6H_2O$. H-LDH exhibits a polyhedron structure, which is assembled by the stacking of ultrathin nanosheets, and well retains the morphology and dimensions of the original ZIF-67 crystals (Figure 2a). With the addition of CuS, CuS-LDH-10 (Figure 2b) and CuS-LDH-20 (Figure 2c) could also maintain their respective polyhedron structures, indicating the stronger template effect of CuS@ZIF-67-10 and CuS@ZIF-67-20 than CuS during the transformation process. The TEM image exhibits that CuS-LDH-10 possesses loose spherical subunits composed of interlaced fine nanosheets. By contrast, CuS-LDH-30 shows similar morphology to the CuS nanoboxes, and the vertically aligned NiCo-LDH nanosheets are grown on the surface of the CuS shells, which demonstrates that the growth of nanosheets is dependent upon the CuS template and several CuS nanocages might be contained in CuS@ZIF-67s during the growth process (Figure 2d). Energy-dispersive X-ray spectroscopy (EDS) mappings of CuS-LDHs can prove the presence of Ni, Co, Cu, S, and O elements
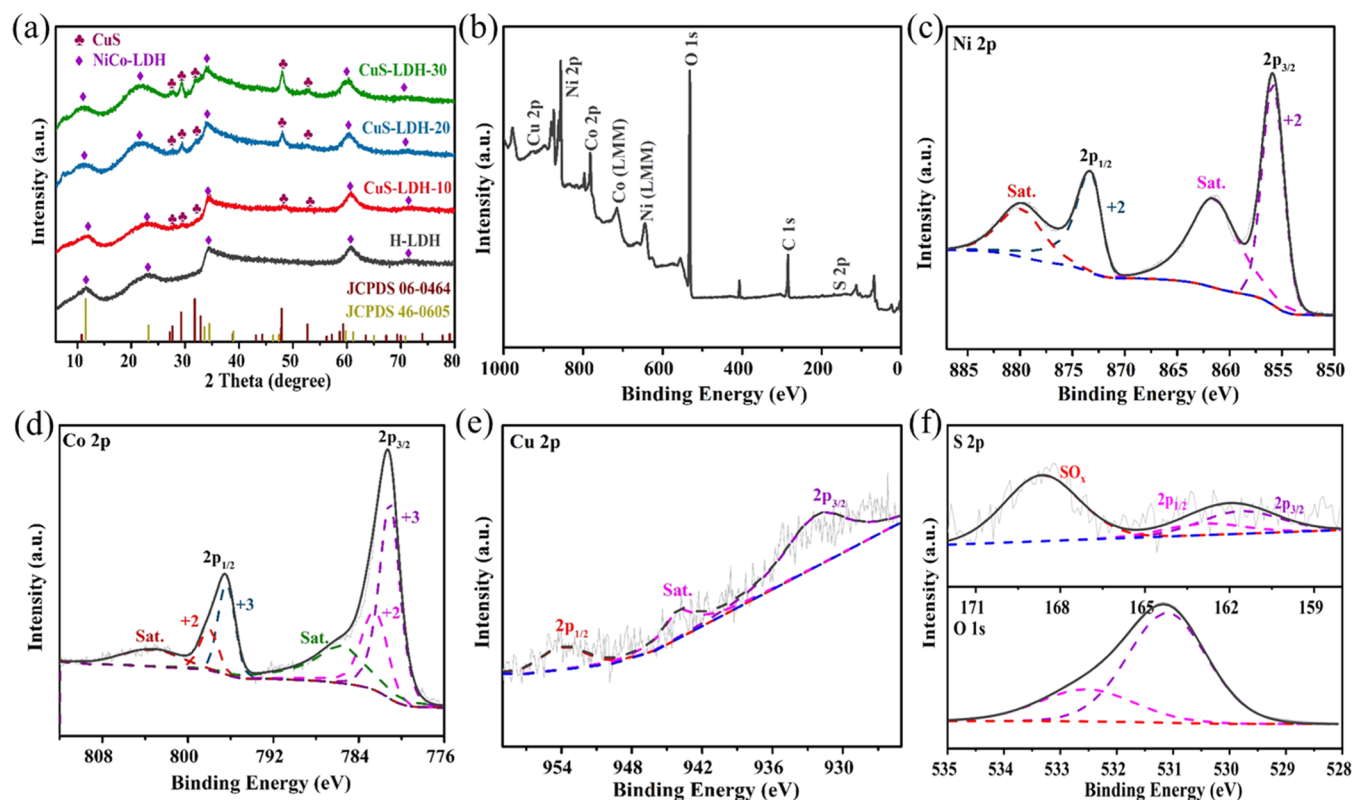
Figure 3. Analysis of CuS-LDH-10. (a) XRD patterns; (b) X-ray photoelectron spectroscopy (XPS) spectrum; and (c) Ni 2p, (d) Co 2p, (e) Cu 2p, and (f) S 2p and O 1s high-resolution XPS spectra.
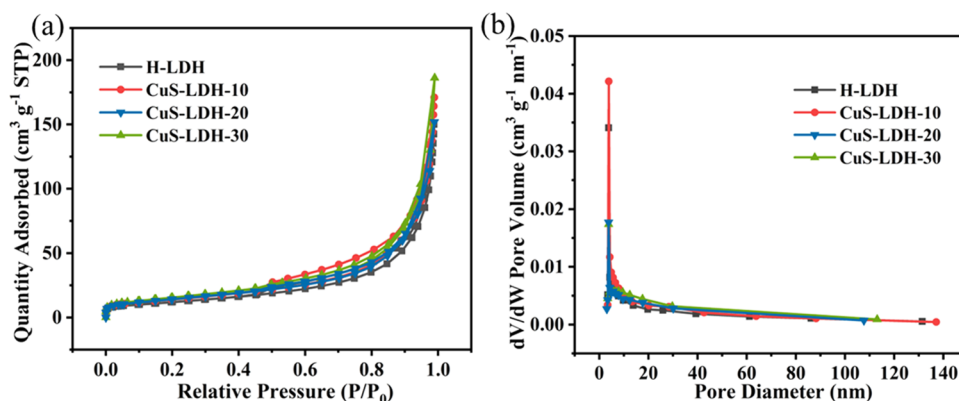

Figure 4. N_2 sorption isotherms (a) and PSD curves (b) of H-LDH, CuS-LDH-10, CuS-LDH-20, and CuS-LDH-30.

(Figures 2e,f andS3); besides, Cu and S are homogeneously dispersed in the samples, implying that the CuS nanoboxes might be broken into fragments. Thus, during the growth of ZIF-67, single or multiple CuS nanoboxes might be included inside the ZIF crystals. With a relatively low addition amount (i.e., 10 mg and 20 mg) of CuS, the sizes of CuS@ZIF-67-10 and CuS@ZIF-67-20 are much larger than the CuS nanoboxes; thus, the formed CuS-LDH-10 and CuS-LDH-20 could retain the similar polyhedron structures of the respective precursors. Furthermore, the particle size of CuS@ZIF-67-30 is slightly larger than that of CuS nanoboxes; thus, the nanosheets are more likely generated relying on the morphology and structure of CuS. As a result, CuS-LDH-30 could possess cubic, multicubic stacked, and broken cubic structures due to the fragmentation of the CuS nanoboxes. The existence of irregular cubic structures further identifies the uniform distribution of

CuS flakes in CuS-LDH-10 and CuS-LDH-20, which could enhance structural stability. These structural and compositional characteristics of CuS-LDHs could provide a more sufficient contact area, facilitate the ion transfer between electrolyte and active material, and enhance the electroconductivity and structural stability.

The as-prepared samples were characterized using XRD to analyze their phase compositions, as displayed in Figure 3a. Definite characteristic diffraction peaks can be observed at 2θ = 11.06, 21.86, 34.12, 59.88, and 71.08 indexed to the (003), (006), (102), (110), and (202) plane reflections of the typical NiCo-LDH materials (JCPDS 46-0605).[50,51] CuS-LDHs show the diffraction peaks of the hydrotalcite-like NiCo-LDH phase; besides, several new distinct diffraction peaks at 27.68, 29.34, 31.8, 48.04, and 52.6 indexed to (101), (102), (103), (110), and (108) crystal planes of CuS (JCPDS 06-0464)
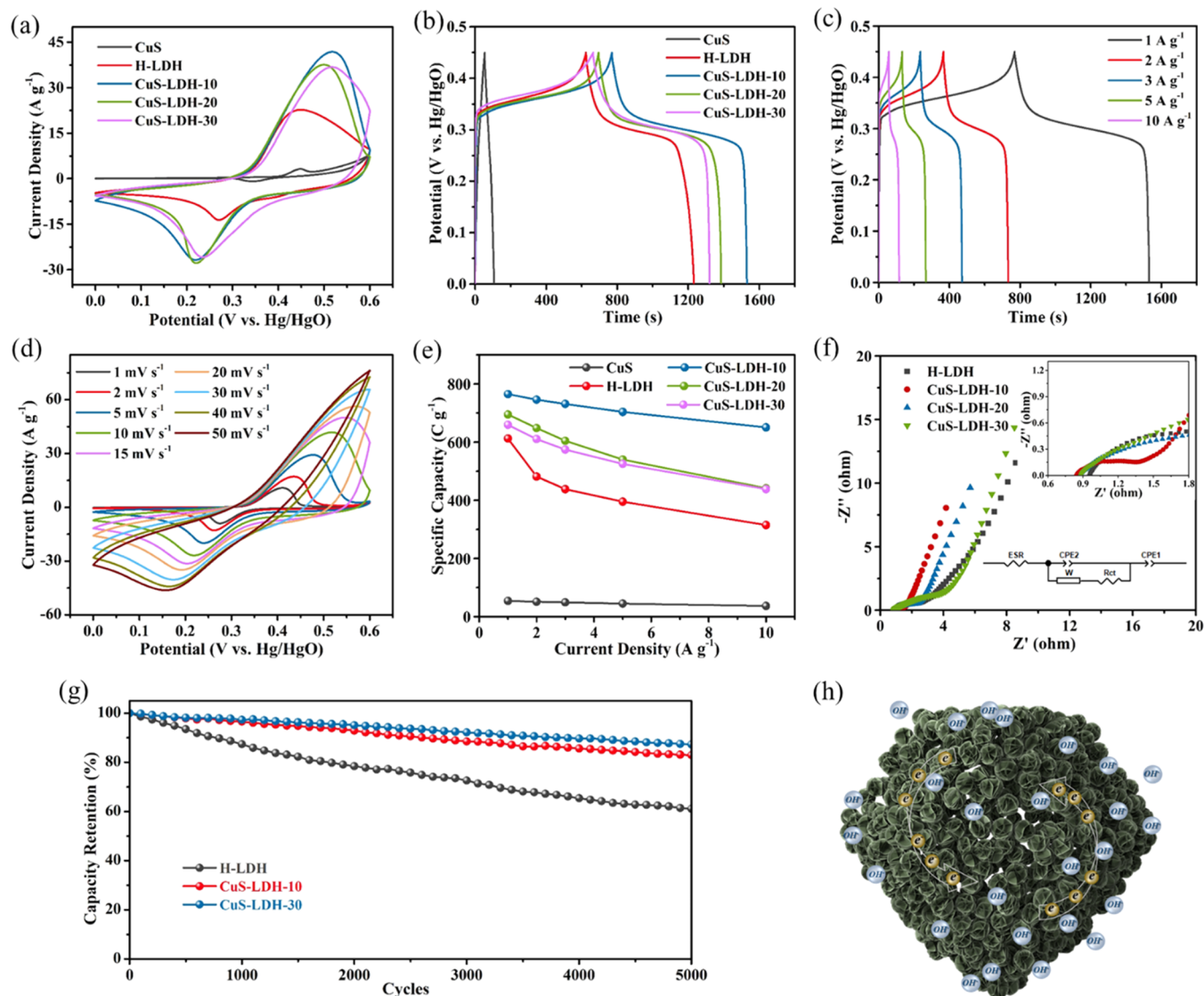
Figure 5. (a) CV curves at 10 mV s^{-1}, (b) GCD curves at 1 A g^{-1}, (c) GCD curves of CuS-LDH-10, (d) CV curves of CuS-LDH-10, (e) specific capacities, (f) Nyquist plots, (g) cycling performance of as-prepared samples, and (h) the schematic of charge transfer of CuS-LDH-10.

appear,[46−48] indicating that the CuS-LDH composite materials contain both the NiCo-LDH and CuS phases.

The elemental compositions and chemical states of as-synthesized samples were studied via X-ray photoelectron spectroscopy (XPS). The XPS spectrum of CuS-LDH-10 (Figure 3b) also confirms the presence of Ni, Co, Cu, S, and O. As shown in Figure 3c, the Ni 2p spectra of CuS-LDH-10 can be fitted well with two shake-up satellites (denoted as "Sat.") and a significant spin−orbit bimodal located at 855.6 eV (Ni 2p$_{3/2}$) and 873.1 eV (Ni 2p$_{1/2}$), which are designated to the signals of Ni^{2+}.[52,53] The Co 2p spectrum (Figure 3d) is deconvolved into two spin−orbit doublet peaks and two shake-up satellites. The deconvoluted peaks at 781.1 and 796.4 eV correspond to Co^{3+}, and the peaks at 782.1 and 798.1 eV are attributed to the Co^{2+} valance state.[54−56] The deconvoluted Cu 2p spectrum (Figure 3e) presents two characteristic peaks, and the distinguished peaks at 932.1 eV (Cu 2p$_{3/2}$) and 953.8 eV (Cu 2p$_{1/2}$) are related to Cu^{2+} in CuS.[57,58] In the S 2p spectra (Figure 3f), the two diffraction peaks at 161.4 and 162.8 eV are associated with S 2p$_{3/2}$ and S 2p$_{1/2}$ of CuS,[57,58] respectively, and the two diffraction peaks of the O 1s

spectrum are attributed to the signals of O^{2-}. In addition, Figures S4 and S5 show that CuS-LDH-20 and CuS-LDH-30 have similar elemental compositions and chemical states to those of CuS-LDH-10.

The specific surface area and porous properties of the samples were obtained via a N$_2$ adsorption/desorption test. All the samples show type-IV isotherms with H3 hysteresis loops (Figure 4a), implying their mesoporous structure.[59,60] Table S1 shows the detailed porosity parameters of the samples. The Brunauer−Emmett−Teller (BET) specific surface area of H-LDH, CuS-LDH-10, CuS-LDH-20, and CuS-LDH-30 is 42.6, 50.7, 51.6, and 56.6 m^2 g^{-1}, respectively. The pore size distribution (PSD, Figure 4b) further reveals the mesoporous features of H-LDH, CuS-LDH-10, CuS-LDH-20, and CuS-LDH-30, and their main pore sizes are ca. 3.84, 3.86, 3.80, and 3.82 nm, respectively. The mesoporous structure could accelerate the transformation of electrolyte ions and alleviate the volume change during the energy storage process. Moreover, the larger specific surface area of CuS-LDHs could enhance the electroactive sites and accessible surface
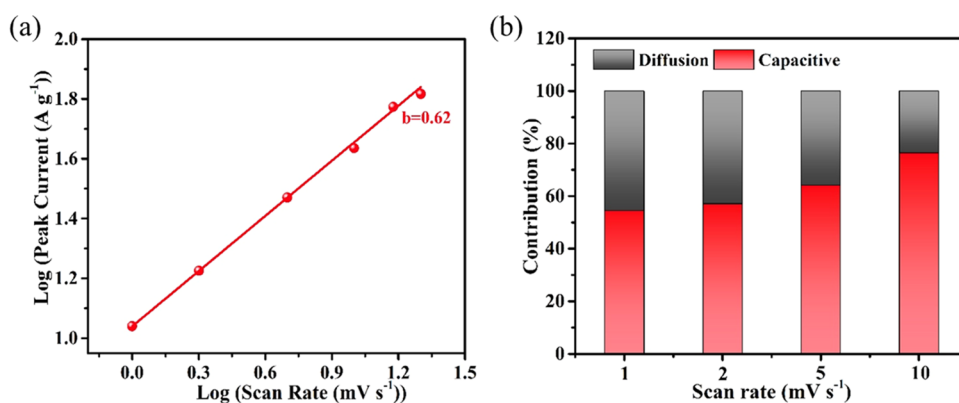
Figure 6. Linear relation of log(i) with log(ν) (a) and ratios of capacitive and diffusion contributions (b) of CuS-LDH-10.

of the electrolyte ions, thus resulting in the improved electrochemical performance of the electrode materials.[61,62]

2.2. Electrochemical Properties of the As-Prepared Materials. The supercapacitor performance of the synthesized samples was studied using a three-electrode system in a 2 M KOH electrolyte. Figure 5a displays the cyclic voltammetry (CV) curves of H-LDH, CuS, CuS-LDH-10, CuS-LDH-20, and CuS-LDH-30 at the scan rate of 10 mV s^{-1} in the potential window of 0−0.6 V (vs Hg/HgO). Obviously, all of the CV curves present a couple of redox peaks with good symmetry, demonstrating the existence of redox reactions on the electrodes and their excellent redox reversibility.[63] CuS-LDH-10 possesses the largest peak current and CV loop area compared with H-LDH, CuS, CuS-LDH-20, and CuS-LDH-30, indicating that CuS-LDH-10 possesses the highest specific capacity.[64−66] The redox reactions related to CuS and NiCo-LDH could be described as follows[39,50]
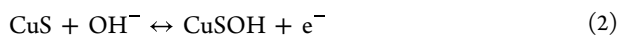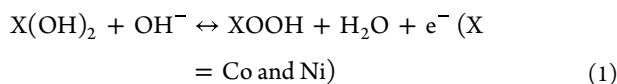
$$X(OH)_2 + OH^- \leftrightarrow XOOH + H_2O + e^- \ (X = Co \ and \ Ni) \quad (1)$$

$$CuS + OH^- \leftrightarrow CuSOH + e^- \quad (2)$$

Figure 5b reveals the galvanostatic charge−discharge (GCD) curves of H-LDH, CuS, CuS-LDH-10, CuS-LDH-20, and CuS-LDH-30 at 1 A g^{-1}. The GCD curves of all samples are nonlinear with obvious potential plateaus; the approximately vertical part is parallel to the capacitive behavior, and a part of the potential plateaus belongs to the faradaic behavior, implying the typical battery-type features of as-prepared materials.[27] The calculated specific capacity values of H-LDH, CuS, CuS-LDH-10, CuS-LDH-20, and CuS-LDH-30 at 1 A g^{-1} are 612.5, 53.9, 765.1, 695.0, and 659.6 C g^{-1}, respectively. CuS-LDH-10 shows higher capacity than most previously reported battery-type materials, as displayed in Table S2. Additionally, Figure 5c reveals the GCD curves of CuS-LDH-10 from 1 to 10 A g^{-1}. The specific capacity of CuS-LDH-10 at 1, 2, 3, 5, and 10 A g^{-1} is 765.1, 745.9, 731.4, 703.9, and 650.7 C g^{-1}, respectively. CuS-LDH-10 can achieve the capacity retention of 85.05% from 1 to 10 A g^{-1}. The GCD curves and specific capacity of H-LDH, CuS, CuS-LDH-20, and CuS-LDH-30 are presented in Figures S6 and 5e, respectively. The capacity retention of H-LDH, CuS, CuS-LDH-20, and CuS-LDH-30 is 51.48, 68.09, 63.53, and 66.49% from 1 to 10 A g^{-1}. Figure 5d shows the CV curves of CuS-LDH-10 from 1 to 50 mV s^{-1}, and a pair of clearly defined redox peaks are more obvious at low scan rates. Furthermore,

due to the polarization effect of the electrode, the cathodic peaks transfer to lower potential, and the anodic peaks move toward higher potential with increasing scan rate.[67] Similar CV curves of H-LDH, CuS-LDH-20, and CuS-LDH-30 are found in Figure S7.

The internal resistances and reaction kinetics of the electrode materials were evaluated using electrochemical impedance spectra (EIS). The corresponding Nyquist plots and equivalent circuits are displayed in Figure 5f. The value of equivalent series resistance (R_s) is equal to the intercept of the fitting curve with the real axis in the high-frequency section. The measured semicircle diameter represents charge transfer resistance (R_{ct}), and the slope of the line in the low-frequency section could indicate the ion diffusion resistance (R_w).[68] The R_s values of CuS-LDH-10, CuS-LDH-20, and CuS-LDH-30 are 0.84, 0.87, and 0.88 Ω, respectively, which are smaller than that of H-LDH (0.95 Ω). Besides, CuS-LDH-10 possesses the semicircle with the smallest diameter and a straight line with the largest slope, suggesting the lowest R_{ct} and R_w. Such results indicate that CuS-LDH-10 has the smallest electrolyte ion transfer resistance and electrochemical reaction resistance.

The cycling performance of the prepared electrodes was evaluated using GCD at 10 A g^{-1} (Figure 5g). After 5000 cycles, CuS-LDH-10 and CuS-LDH-30 have capacity retention values of ca. 82.9 and 87.3%, respectively, which are significantly higher than that of H-LDH (61.1%). It can thus be proved that CuS-LDH-10 and CuS-LDH-30 possess excellent cycling stability owing to the advantages of the composition and structure of the CuS-LDH composite materials. CuS-LDH-10 can retain the nanosheet structure, but some damaged and collapsed structures can also be found, as shown in Figure S8.

The superior electrochemical properties of the CuS-LDH-10 composite should be associated with its unique structures and compositions, and the charge transfer of CuS-LDH-10 is demonstrated in Figure 5h. First, the CuS-LDH composite material with uniform distribution of CuS can enhance structural stability and electrochemical conductivity. Second, the hollow CuS-LDH-10 material possesses loose spherical subunits composed of interlaced fine nanosheets, which could provide a more sufficient contact area and facilitate the ion transfer between electrolyte and active material. Finally, the high specific surface area and the mesoporous feature can promise the rapid transport of ions and charges, as well as buffer the volume change during the energy storage process. Thus, the CuS-LDH-10 composite electrode material can realize excellent electrochemical performance.
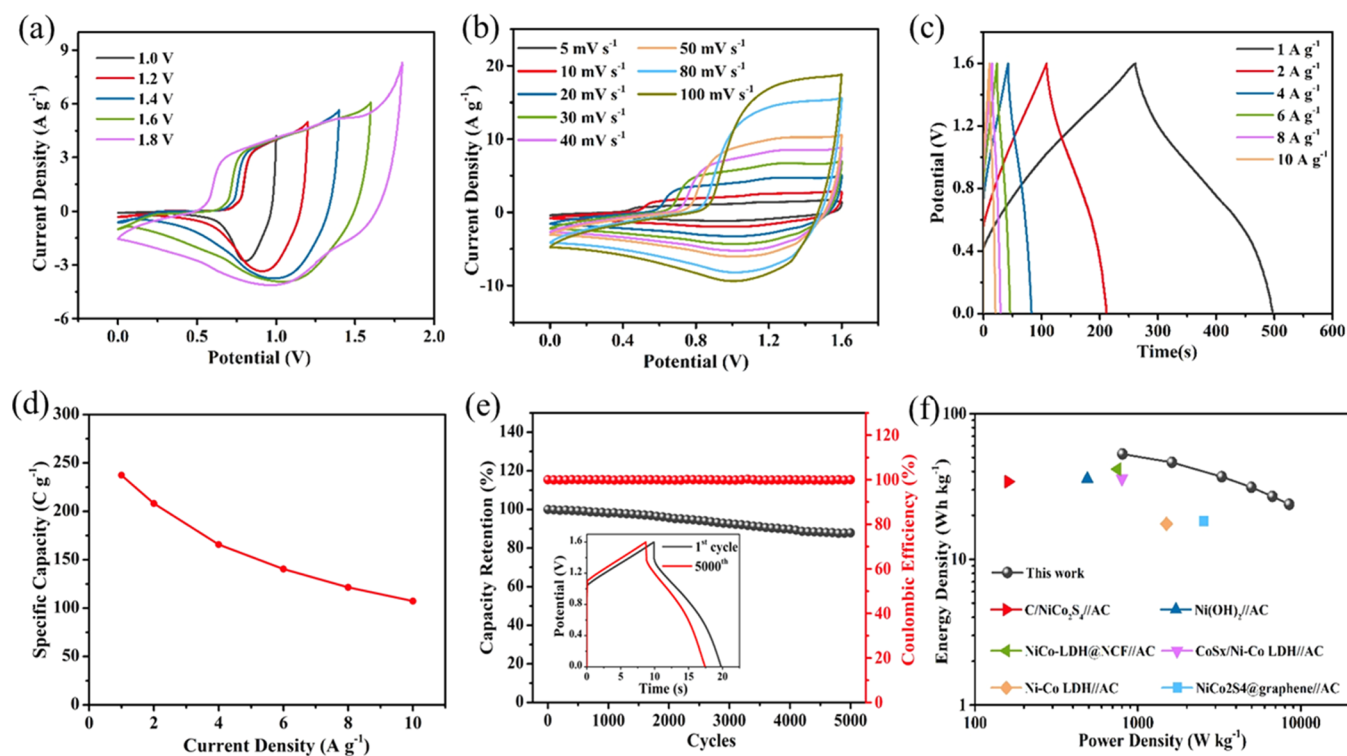
Figure 7. Electrochemical performance of the CuS-LDH-10//AC HSC device: (a) CV curves at different voltage windows at 10 mV s⁻¹, (b) CV curves, (c) GCD curves, (d) specific capacity at different current densities, (e) cycling performance, and (f) Ragone plots.

The electrochemical reaction kinetics of electrode material could be analyzed by a CV test. The relationship between peak currents (i) and scan rate (v) could be calculated by the following equation[69,70]

$$\log(i) = b \log(v) + \log a \quad (3)$$

where a and b are both undetermined constants. The b value is evaluated by the slope of the fitted line of $\log(v)$ vs $\log(i)$, as displayed in Figure 6a. Herein, $b = 0.5$ represents the electrochemical reactions of the electrode dominated by the diffusion-controlled process, while $b = 1$ indicates totally surface capacitive behaviors of the electrode material.[69,70] The corresponding b value for anodic peaks of CuS-LDH-10 is 0.62, demonstrating that the material is affected by both surface capacitive behaviors and the diffusion process during the energy storage process. Additionally, the respective contribution for the full capacity is further calculated by eq 4.[19]

$$i(V) = k_1 v + k_2 v^{1/2} \quad (4)$$

where $k_1 v$ and $k_2 v^{1/2}$ represent the capacitive and diffusion contributions, respectively. As shown in Figure 6b, the ratios of the capacitive contribution of the CuS-LDH-10 electrode are 54.5, 57.1, 64.1, and 76.4% at scan rates of 1, 2, 5, and 10 mV s⁻¹, respectively.

2.3. Electrochemical Properties of the CuS-LDH-10// Active Carbon HSC Device. To explore the practical performance of the prepared CuS-LDH-10 material, a HSC was assembled using CuS-LDH-10 as the cathode and active carbon (AC) as the anode in a 2 M KOH electrolyte. Figure S9a,b shows the electrochemical measurements of AC within −1.0 to 0 V. The specific capacitances of AC are calculated as 187.2, 168.2, 156.4, 150.7, 149.3, and 147.6 F g⁻¹ at 1, 2, 5, 10, 15, and 20 A g⁻¹, respectively. Likewise, Figure S9c presents

the CV curves of AC negative material and CuS-LDH-10 positive material; thus, the voltage of the fabricated HSC could be increased to 1.6 V. To validate such a claim, the CV curves of the HSC (Figure 7a) were tested from 0−1.0 to 0−1.8 V. It could be seen that the assembled HCS can maintain stable operational voltage up to 1.6 V without an obvious oxygen evolution reaction.

Figure 7b demonstrates the CV curves of the tested HSC at various scan rates; the CV curves combine the characteristics of both capacitive and faradaic behaviors. They can maintain similar shapes without obvious deformation from 5 to 100 mV s⁻¹, demonstrating the high reversibility and superb rate capability of the HSC device. All of the GCD curves (Figure 7c) have good symmetry, indicating the excellent coulombic efficiency and redox reversibility of the device. The calculated specific capacities of the HSC device (Figure 7d) are 237.3, 208.1, 165.7, 140.4, 121.5, and 107.3 C g⁻¹ at 1, 2, 4, 6, 8, and 10 A g⁻¹, respectively. The cycle performance of the CuS-LDH-10//AC supercapacitor device was evaluated using GCD at 10 A g⁻¹, as displayed in Figure 7e. The result exhibits that the CuS-LDH-10//AC device delivers 87.9% capacity retention after 5000 cycles and maintains almost 100% coulombic efficiency, proving the excellent cycle performance and the charge−discharge efficiency of the as-prepared HSC.

The Ragone plot (Figure 7f) of the assembled HSC demonstrates a maximum energy density of 52.7 Wh kg⁻¹ at a power density of 804.5 W kg⁻¹, and the energy density can be maintained at 23.8 Wh kg⁻¹ even at a power density of 8482.4 W kg⁻¹. The properties of the assembled HSC are better than those of previous reports, such as CoS$_x$/Ni-Co LDH//AC,[71] Ni(OH)$_2$//AC,[72] Ni-Co LDH//AC,[73] NiCo-LDH@NCF// AC,[74] C/NiCo$_2$S$_4$//AC,[75] and NiCo$_2$S$_4$@graphene//porous carbon.[76] Consequently, the assembled HSC has excellent

electrochemical performance and enormous potential in practical applications of energy storage devices.

3. CONCLUSIONS

Hollow CuS-LDH composite materials were synthesized by an effective and facile strategy. Different morphologies and structures were successfully fabricated according to the additive amounts of CuS. CuS-LDH-10 with uniformly dispersed CuS prepared using CuS@ZIF-67-10 as the precursor and a sacrificial template shows a unique hollow polyhedral structure constituted by loose nanosphere units, and these nanosphere units are composed of interlaced fine nanosheets, while the vertically aligned NiCo-LDH nanosheets of CuS-LDH-30 are grown on the surface of the CuS shells to create the hollow cubic morphology. The CuS-LDH-10 and CuS-LDH-30 electrodes possess excellent electrochemical properties, exhibiting high capacity performance (765.1 and 659.6 C g^{-1} at 1 A g^{-1}, respectively), superior rate capability, and high cycle stability. The assembled hybrid supercapacitor (CuS-LDH-10//AC) delivers a maximum energy density of 52.7 Wh kg^{-1} at 804.5 W kg^{-1} and exhibits good cycling performance (87.9% capacity retention after 5000 cycles). The present work may offer facile and effective routes for the exploitation of unique hollow metal sulfide/hydroxide composite electrode materials for high-performance energy storage devices.

4. EXPERIMENTAL SECTION

4.1. Preparation of CuS Nanoboxes. The Cu_2O nanocubes were crafted using a procedure similar to that reported in the literature with minor modifications.[77] Typically, 30.0 mL of NaOH aqueous solution (2.0 mol L^{-1}) was dropped into 300 mL of $CuCl_2 \cdot 2H_2O$ aqueous solution (0.01 mol L^{-1}) with stirring for 0.5 h. Then, 30 mL of ascorbic acid solution (0.6 mol L^{-1}) was blended into the mixture and stirred for another 3 h. After washing and drying, the obtained precipitate was Cu_2O nanoboxes. The above procedures were carried out in a water bath at 50 °C. Next, 80 mg of as-prepared Cu_2O nanocubes was dispersed in 60 mL of methanol, and 4 mL of Na_2S solution (0.1 mol L^{-1}) was then mixed. The precipitate was centrifuged and washed with C_2H_5OH after stirring for 10 min. Likewise, the as-obtained $Cu_2O@CuS$ nanocubes were dispersed in 60 mL of CH_3OH and mixed with 10 mL of HCl (2 mol L^{-1}). The mixture was stirred for 30 min to collect the CuS nanoboxes after a centrifugal rinse with C_2H_5OH and drying at 60 °C overnight.

4.2. Preparation of CuS@ZIF-67s. Typically, 10 mg of CuS nanoboxes was dispersed in 20 mL of methanol/H_2O solvent (volume ratio = 1: 1). Then, 1 mmol of $Co(NO_3)_2 \cdot 6H_2O$ was poured into the solution with stirring for 30 min to form solution A. Approximately 8 mmol of $C_4H_6N_2$ was dissolved in 20 mL of H_2O with stirring for 30 min to form solution B, which was then poured into solution A with stirring for another 15 min. After 5 h of aging, the precipitate was centrifuged and washed with C_2H_5OH and dried at 60 °C overnight to obtain CuS@ZIF-67-10. The as-prepared samples for 20 mg and 30 mg of CuS were labeled as CuS@ZIF-67-20 and CuS@ZIF-67-30, respectively. In addition, ZIF-67 was prepared using the same process without CuS.

4.3. Preparation of CuS-LDHs. Typically, 80 mg of CuS@ZIF-67-10 was uniformly dispersed in 20 mL of C_2H_5OH, followed by the addition of 10 mL of C_2H_5OH

containing 320 mg of $Ni(NO_3)_2 \cdot 6H_2O$. After stirring for 1 h, CuS-LDH-10 was collected by centrifugal washing with C_2H_5OH and drying at 60 °C overnight. H-LDH (ZIF-67), CuS-LDH-20 (CuS@ZIF-67-20), and CuS-LDH-30 (CuS@ZIF-67-30) were also prepared successfully using a similar procedure.

■ ASSOCIATED CONTENT

ⓈI Supporting Information

The Supporting Information is available free of charge at https://pubs.acs.org/doi/10.1021/acsomega.2c03511.

> Materials; characterization method; electrode preparation in this study; porosity parameters of CuS-LDHs; comparison of capacity; SEM images and XRD patterns of Cu_2O and CuS; EDS elemental mapping images of CuS-LDH-20; XPS spectra of CuS-LDH-20 and CuS-LDH-30; GCD and CV curves of H-LDH, CuS, CuS-LDH-20, and CuS-LDH-30 at various current densities and scan rates; SEM image after the cycling test; and electrochemical properties of AC (PDF)

■ AUTHOR INFORMATION

Corresponding Author

Xiongchao Lin − *School of Chemical & Environmental Engineering, China University of Mining and Technology (Beijing), Beijing 100083, P. R. China;* ⓞ orcid.org/0000-0003-1370-7059; Email: lxc@cumtb.edu.cn

Authors

Zhe Sheng − *School of Chemical & Environmental Engineering, China University of Mining and Technology (Beijing), Beijing 100083, P. R. China*

Yiting Zhao − *School of Chemical & Environmental Engineering, China University of Mining and Technology (Beijing), Beijing 100083, P. R. China*

Lei Huang − *School of Chemical & Environmental Engineering, China University of Mining and Technology (Beijing), Beijing 100083, P. R. China*

Hongfeng Gao − *School of Chemical & Environmental Engineering, China University of Mining and Technology (Beijing), Beijing 100083, P. R. China*

Hao Wei − *School of Chemical & Environmental Engineering, China University of Mining and Technology (Beijing), Beijing 100083, P. R. China*

Caihong Wang − *School of Chemical & Environmental Engineering, China University of Mining and Technology (Beijing), Beijing 100083, P. R. China*

Deping Xu − *School of Chemical & Environmental Engineering, China University of Mining and Technology (Beijing), Beijing 100083, P. R. China*

Yonggang Wang − *School of Chemical & Environmental Engineering, China University of Mining and Technology (Beijing), Beijing 100083, P. R. China;* ⓞ orcid.org/0000-0003-3364-4112

Complete contact information is available at:
https://pubs.acs.org/10.1021/acsomega.2c03511

Notes

The authors declare no competing financial interest.

■ ACKNOWLEDGMENTS

■ REFERENCES

(1) Krishnamoorthy, K.; Pazhamalai, P.; Mariappan, V. K.; Nardekar, S. S.; Sahoo, S.; Kim, S. J. Probing the Energy Conversion Process in Piezoelectric-Driven Electrochemical Self-Charging Supercapacitor Power Cell Using Piezoelectrochemical Spectroscopy. *Nat. Commun.* **2020**, *11*, No. 2351.

(2) Sun, J.; Xu, C.; Chen, H. A Review on the Synthesis of CuCo$_2$O$_4$-Based Electrode Materials and Their Applications in Supercapacitors. *J. Materiomics* **2021**, *7*, 98−126.

(3) Wu, R.; Sun, J.; Xu, C.; Chen, H. MgCo$_2$O$_4$-Based Electrode Materials for Electrochemical Energy Storage and Conversion: A Comprehensive Review. *Sustainable Energy Fuels* **2021**, *5*, 4807−4829.

(4) Qin, H.; Liu, P.; Chen, C.; Cong, H. P.; Yu, S. H. A Multi-Responsive Healable Supercapacitor. *Nat. Commun.* **2021**, *12*, No. 4297.

(5) Wang, M.; Han, K.; Qi, J.; Teng, Z.; Zhang, J.; Li, M. Study on Performance and Charging Dynamics of N/O Codoped Layered Porous Carbons Derived from L-Tyrosine for Supercapacitors. *Appl. Surf. Sci.* **2022**, *578*, No. 151888.

(6) Javed, M. S.; Lei, H.; Li, J.; Wang, Z.; Mai, W. Construction of Highly Dispersed Mesoporous Bimetallic-Sulfide Nanoparticles Locked in N-Doped Graphitic Carbon Nanosheets for High Energy Density Hybrid Flexible Pseudocapacitors. *J. Mater. Chem. A* **2019**, *7*, 17435−17445.

(7) Cheng, Z.; Wang, Z.; Wu, P.; Wang, Y.; Fu, J. Mass Fabrication of Oxygen and Nitrogen Co-Doped 3D Hierarchical Porous Carbon Nanosheets by an Explosion-Assisted Strategy for Supercapacitor and Dye Adsorption Application. *Appl. Surf. Sci.* **2020**, *529*, No. 147079.

(8) Chen, L.; Wan, J.; Fan, L.; Wei, Y.; Zou, J. Construction of CoNi$_2$S$_4$ Hollow Cube Structures for Excellent Performance Asymmetric Supercapacitors. *Appl. Surf. Sci.* **2021**, *570*, No. 151174.

(9) Zhang, Q.; Han, K.; Li, S.; Li, M.; Li, J.; Ren, K. Synthesis of Garlic Skin-Derived 3D Hierarchical Porous Carbon for High-Performance Supercapacitors. *Nanoscale* **2018**, *10*, 2427−2437.

(10) Kirubasankar, B.; Palanisamy, P.; Arunachalam, S.; Murugadoss, V.; Angaiah, S. 2D MoSe$_2$-Ni(OH)$_2$ Nanohybrid as an Efficient Electrode Material with High Rate Capability for Asymmetric Supercapacitor Applications. *Chem. Eng. J.* **2019**, *355*, 881−890.

(11) Peng, Z.; Yang, C.; Hu, Y.; Bai, F.; Chen, W.; Liu, R.; Jiang, S.; Chen, H. C. Double-Shelled Mn-Doped NiCo$_2$S$_4$ Hollow Nanowire Arrays for High-Reactivity Hybrid Supercapacitors. *Appl. Surf. Sci.* **2022**, *573*, No. 151561.

(12) Zhou, J.; Zhang, S.; Zhou, Y. N.; Tang, W.; Yang, J.; Peng, C.; Guo, Z. Biomass-Derived Carbon Materials for High-Performance Supercapacitors: Current Status and Perspective. *Electrochem. Energy Rev.* **2021**, *4*, 219−248.

(13) Xu, Z.; Deng, W.; Wang, X. 3D Hierarchical Carbon-Rich Micro-/Nanomaterials for Energy Storage and Catalysis. *Electrochem. Energy Rev.* **2021**, *4*, 269−335.

(14) Yu, Z.; Tetard, L.; Zhai, L.; Thomas, J. Supercapacitor Electrode Materials: Nanostructures from 0 to 3 Dimensions. *Energy Environ. Sci.* **2015**, *8*, 702−730.

(15) Yang, Z.; Li, W.; Zhang, G.; Wang, J.; Zuo, J.; Xu, Q.; Shan, H.; He, X.; Lv, M.; Hu, J.; Huang, W.; Zhang, J.; Li, X. Constructing Sb-O-C Bond to Improve the Alloying Reaction Reversibility of Free-Standing Sb$_2$Se$_3$ Nanorods for Potassium-Ion Batteries. *Nano Energy* **2022**, *93*, No. 106764.

(16) Guan, C.; Liu, X.; Ren, W.; Li, X.; Cheng, C.; Wang, J. Rational Design of Metal-Organic Framework Derived Hollow NiCo$_2$O$_4$ Arrays for Flexible Supercapacitor and Electrocatalysis. *Adv. Energy Mater.* **2017**, *7*, No. 1602391.

(17) Gao, X.; Zhang, R.; Huang, X.; Shi, Y.; Wang, C.; Gao, Y.; Han, Z. One-Step Growth of NiCoAl Layered Double Hydroxides Microspheres toward High Energy Density Supercapacitors. *J. Alloys Compd.* **2021**, *859*, No. 157879.

(18) Chen, H.; Jiang, J.; Zhang, L.; Xia, D.; Zhao, Y.; Guo, D.; Qi, T.; Wan, H. In Situ Growth of NiCo$_2$S$_4$ Nanotube Arrays on Ni Foam for Supercapacitors: Maximizing Utilization Efficiency at High Mass Loading to Achieve Ultrahigh Areal Pseudocapacitance. *J. Power Sources* **2014**, *254*, 249−257.

(19) Dang, T.; Wei, D.; Zhang, G.; Wang, L.; Li, Q.; Liu, H.; Cao, Z.; Zhang, G.; Duan, H. Homologous NiCoP/CoP Hetero-Nano-sheets Supported on N-Doped Carbon Nanotubes for High-Rate Hybrid Supercapacitors. *Electrochim. Acta* **2020**, *341*, No. 135988.

(20) Wang, X.; Huang, F.; Rong, F.; He, P.; Que, R.; Jiang, S. P. Unique MOF-Derived Hierarchical MnO$_2$ Nanotubes@NiCo-LDH/CoS$_2$ Nanocage Materials as High Performance Supercapacitors. *J. Mater. Chem. A* **2019**, *7*, No. 12018.

(21) Tian, J.; Zang, Y.; Sun, J.; Qu, J.; Gao, F.; Liang, G. Surface Charge Density-Dependent Performance of Ni−Al Layered Double Hydroxide-Based Flexible Self-Powered Generators Driven by Natural Water Evaporation. *Nano Energy* **2020**, *70*, No. 104502.

(22) Yang, J.; Yu, C.; Hu, C.; Wang, M.; Li, S.; Huang, H.; Bustillo, K.; Han, X.; Zhao, C.; Guo, W.; Zeng, Z.; Zheng, H.; Qiu, J. Surface-Confined Fabrication of Ultrathin Nickel Cobalt-Layered Double Hydroxide Nanosheets for High-Performance Supercapacitors. *Adv. Funct. Mater.* **2018**, *28*, No. 1803272.

(23) Zhang, X.; Lu, W.; Tian, Y.; Yang, S.; Zhang, Q.; Lei, D.; Zhao, Y. Nanosheet-Assembled NiCo-LDH Hollow Spheres as High-Performance Electrodes for Supercapacitors. *J. Colloid Interface Sci.* **2022**, *606*, 1120−1127.

(24) Yang, J.; Yu, C.; Fan, X.; Qiu, J. 3D Architecture Materials Made of NiCoAl-LDH Nanoplates Coupled with NiCo-Carbonate Hydroxide Nanowires Grown on Flexible Graphite Paper for Asymmetric Supercapacitors. *Adv. Energy Mater.* **2014**, *4*, No. 1400761.

(25) Chen, F.; Wang, H.; Ji, S.; Linkov, V.; Wang, R. Core-Shell Structured Ni$_3$S$_2$@Co(OH)$_2$ Nano-Wires Grown on Ni Foam as Binder-Free Electrode for Asymmetric Supercapacitors. *Chem. Eng. J.* **2018**, *345*, 48−57.

(26) Chen, A.; Li, Y.; Liu, L.; Yu, Y.; Xia, K.; Wang, Y.; Li, S. Controllable Synthesis of Nitrogen-Doped Hollow Mesoporous Carbon Spheres Using Ionic Liquids as Template for Supercapacitors. *Appl. Surf. Sci.* **2017**, *393*, 151−158.

(27) Lee, G.; Na, W.; Kim, J.; Lee, S.; Jang, J. Improved Electrochemical Performances of MOF-Derived Ni-Co Layered Double Hydroxide Complexes Using Distinctive Hollow-in-Hollow Structures. *J. Mater. Chem. A* **2019**, *7*, No. 17637.

(28) Wu, G.; Huang, J.; Zang, Y.; He, J.; Xu, G. Porous Field-Effect Transistors Based on a Semiconductive Metal-Organic Framework. *J. Am. Chem. Soc.* **2017**, *139*, 1360−1363.

(29) Zhang, Z.; Huang, Y.; Li, X.; Gao, X.; Liu, P.; Li, T. Rationally Designed Polyhedral Carbon Framework from Solid to Hollow for Long Cycle Life Secondary Batteries. *J. Mater. Chem. A* **2021**, *9*, 6284−6297.

(30) Salunkhe, R. R.; Kaneti, Y. V.; Yamauchi, Y. Metal-Organic Framework-Derived Nanoporous Metal Oxides toward Supercapacitor Applications: Progress and Prospects. *ACS Nano* **2017**, *11*, 5293−5308.

(31) Jiang, Z.; Lu, W.; Li, Z.; Ho, K. H.; Li, X.; Jiao, X.; Chen, D. Synthesis of Amorphous Cobalt Sulfide Polyhedral Nanocages for High Performance Supercapacitors. *J. Mater. Chem. A* **2014**, *2*, 8603−8606.

(32) Hu, H.; Guan, B.; Xia, B.; Lou, X. W. Designed Formation of Co$_3$O$_4$/NiCo$_2$O$_4$ Double-Shelled Nanocages with Enhanced Pseudo-capacitive and Electrocatalytic Properties. *J. Am. Chem. Soc.* **2015**, *137*, 5590−5595.

(33) Jiang, Z.; Li, Z.; Qin, Z.; Sun, H.; Jiao, X.; Chen, D. LDH Nanocages Synthesized with MOF Templates and Their High Performance as Supercapacitors. *Nanoscale* **2013**, *5*, No. 11770.

(34) Chen, H.; Wang, M. Q.; Yu, Y.; Liu, H.; Lu, S. Y.; Bao, S. J.; Xu, M. Assembling Hollow Cobalt Sulfide Nanocages Array on Graphene-like Manganese Dioxide Nanosheets for Superior Electrochemical Capacitors. *ACS Appl. Mater. Interfaces* **2017**, *9*, 35040−35047.

(35) Guo, X. L.; Zhang, J. M.; Xu, W. N.; Hu, C. G.; Sun, L.; Zhang, Y. X. Growth of NiMn LDH Nanosheet Arrays on KCu_7S_4 Microwires for Hybrid Supercapacitors with Enhanced Electrochemical Performance. *J. Mater. Chem. A* **2017**, *5*, 20579−20587.

(36) Hu, H.; Han, L.; Yu, M.; Wang, Z.; Lou, X. W. Metal-Organic-Framework-Engaged Formation of Co Nanoparticle-Embedded Carbon@Co_9S_8 Double-Shelled Nanocages for Efficient Oxygen Reduction. *Energy Environ. Sci.* **2016**, *9*, 107−111.

(37) Zhao, Y.; Hu, L.; Zhao, S.; Wu, L. Preparation of $MnCo_2O_4$@$Ni(OH)_2$ Core−Shell Flowers for Asymmetric Supercapacitor Materials with Ultrahigh Specific Capacitance. *Adv. Funct. Mater.* **2016**, *26*, 4085−4093.

(38) Li, W.; Song, Q.; Li, M.; Yuan, Y.; Zhang, J.; Wang, N.; Yang, Z.; Huang, J.; Lu, J.; Li, X. Chemical Heterointerface Engineering on Hybrid Electrode Materials for Electrochemical Energy Storage. *Small Methods* **2021**, *5*, No. 2100444.

(39) El-Hout, S. I.; Mohamed, S. G.; Gaber, A.; Attia, S. Y.; Shawky, A.; El-Sheikh, S. M. High Electrochemical Performance of RGO Anchored CuS Nanospheres for Supercapacitor Applications. *J. Energy Storage* **2021**, *34*, No. 102001.

(40) Zhou, W.; Miao, J.; Yan, X.; Li, Y.; Zhu, Y.; Zhang, W.; Zhang, M.; Zhu, W.; Javed, M. S.; Pan, J.; Hussain, S. Boosted Electrochemical Performance of CuS Anchored on Carbon Cloth as an Integrated Electrode for Quasi-Solid-State Flexible Supercapacitor. *J. Electroanal. Chem.* **2021**, *897*, No. 115610.

(41) Jin, K.; Zhou, M.; Zhao, H.; Zhai, S.; Ge, F.; Zhao, Y.; Cai, Z. Electrodeposited CuS Nanosheets on Carbonized Cotton Fabric as Flexible Supercapacitor Electrode for High Energy Storage. *Electrochim. Acta* **2019**, *295*, 668−676.

(42) Liu, Y.; Zhou, Z.; Zhang, S.; Luo, W.; Zhang, G. Controllable Synthesis of CuS Hollow Microflowers Hierarchical Structures for Asymmetric Supercapacitors. *Appl. Surf. Sci.* **2018**, *442*, 711−719.

(43) Liu, X.; Guo, M.; Wei, C.; Ji, X.; Zheng, W. Purposely Synthesis of Hierarchical CuS Nanoflowers Composed of Ultrathin Nanoflakes with Exposed (0 0 1) Facets Using a Solvent-Template Ionic Liquid and Their Application in Supercapacitors. *Mater. Sci. Eng., B* **2021**, *273*, No. 115433.

(44) Fang, Y.; Luan, D.; Chen, Y.; Gao, S.; Lou, X. W. Rationally Designed Three-Layered Cu_2S@Carbon@MoS_2 Hierarchical Nanoboxes for Efficient Sodium Storage. *Angew. Chem., Int. Ed.* **2020**, *59*, 7178−7183.

(45) Li, P.; Zhang, M.; Yin, H.; Yao, J.; Liu, X.; Chen, S. Hierarchical Mesoporous NiCoP Hollow Nanocubes as Efficient and Stable Electrodes for High-Performance Hybrid Supercapacitor. *Appl. Surf. Sci.* **2021**, *536*, No. 147751.

(46) De, B.; Kuila, T.; Kim, N. H.; Lee, J. H. Carbon Dot Stabilized Copper Sulphide Nanoparticles Decorated Graphene Oxide Hydrogel for High Performance Asymmetric Supercapacitor. *Carbon* **2017**, *122*, 247−257.

(47) Zhang, J.; Feng, H.; Yang, J.; Qin, Q.; Fan, H.; Wei, C.; Zheng, W. Solvothermal Synthesis of Three-Dimensional Hierarchical CuS Microspheres from a Cu-Based Ionic Liquid Precursor for High-Performance Asymmetric Supercapacitors. *ACS Appl. Mater. Interfaces* **2015**, *7*, 21735−21744.

(48) Tian, Z.; Dou, H.; Zhang, B.; Fan, W.; Wang, X. Three-Dimensional Graphene Combined with Hierarchical CuS for the Design of Flexible Solid-State Supercapacitors. *Electrochim. Acta* **2017**, *237*, 109−118.

(49) He, P.; Yu, X. Y.; Lou, X. W. D. Carbon-Incorporated Nickel−Cobalt Mixed Metal Phosphide Nanoboxes with Enhanced Electrocatalytic Activity for Oxygen Evolution. *Angew. Chem., Int. Ed.* **2017**, *129*, 1−5.

(50) Tahir, M. U.; Arshad, H.; Zhang, H.; Hou, Z.; Wang, J.; Yang, C.; Su, X. Room Temperature and Aqueous Synthesis of Bimetallic ZIF Derived CoNi Layered Double Hydroxides and Their Applications in Asymmetric Supercapacitors. *J. Colloid Interface Sci.* **2020**, *579*, 195−204.

(51) Zhou, Y.; Li, J.; Yang, Y.; Luo, B.; Zhang, X.; Fong, E.; Chu, W.; Huang, K. Unique 3D Flower-on-Sheet Nanostructure of NiCo LDHs: Controllable Microwave-Assisted Synthesis and Its Application for Advanced Supercapacitors. *J. Alloys Compd.* **2019**, *788*, 1029−1036.

(52) Wang, J.; Huang, Y.; Han, X.; Zhang, S.; Wang, M.; Yan, J.; Chen, C.; Zong, M. Construction of Hierarchical Co_9S_8@NiO Synergistic Microstructure for High-Performance Asymmetric Supercapacitor. *J. Colloid Interface Sci.* **2021**, *603*, 440−449.

(53) Liang, J.; Xiang, C.; Zou, Y.; Hu, X.; Chu, H.; Qiu, S.; Xu, F.; Sun, L. Spacing Graphene and Ni-Co Layered Double Hydroxides with Polypyrrole for High-Performance Supercapacitors. *J. Mater. Sci. Technol.* **2020**, *55*, 190−197.

(54) Xu, L.; Xi, Y.; Li, W.; Hua, Z.; Peng, J.; Hu, J.; Zhou, J. J.; Zhang, P.; Wang, J.; Wang, W.; Ding, H.; Wang, W.; Ji, W.; Yang, Y.; Xu, X.; Chen, L.; Li, X. 3D Frame-like Architecture of N-C-Incorporated Mixed Metal Phosphide Boosting Ultrahigh Energy Density Pouch-Type Supercapacitors. *Nano Energy* **2022**, *91*, No. 106630.

(55) Chen, H.; Liu, Y.; Wu, R.; Liu, X.; Liu, Y.; Xu, C. Battery-Type and Binder-Free $MgCo_2O_4$-NWs@NF Electrode Materials for the Assembly of Advanced Hybrid Supercapacitors. *Int. J. Hydrogen Energy* **2022**, *47*, 15807−15819.

(56) Chen, H.; Du, X.; Liu, X.; Wu, R.; Li, Y.; Xu, C. Facile Growth of Nickel Foam-Supported $MnCo_2O_{4.5}$ Porous Nanowires as Binder-Free Electrodes for High-Performance Hybrid Supercapacitors. *J. Energy Storage* **2022**, *50*, No. 104297.

(57) Zhai, S.; Fan, Z.; Jin, K.; Zhou, M.; Zhao, H.; Zhao, Y.; Ge, F.; Li, X.; Cai, Z. Synthesis of Zinc Sulfide/Copper Sulfide/Porous Carbonized Cotton Nanocomposites for Flexible Supercapacitor and Recyclable Photocatalysis with High Performance. *J. Colloid Interface Sci.* **2020**, *575*, 306−316.

(58) Ma, Y.; Hao, J.; Liu, H.; Shi, W.; Lian, J. Facile Synthesis Clusters of Sheet-like Ni_3S_4/CuS Nanohybrids with Ultrahigh Supercapacitor Performance. *J. Solid State Chem.* **2020**, *282*, No. 121088.

(59) Li, Z.; Huang, Y.; Zhang, Z.; Wang, J.; Han, X.; Zhang, G.; Li, Y. Hollow C-LDH/Co_9S_8 Nanocages Derived from ZIF-67-C for High- Performance Asymmetric Supercapacitors. *J. Colloid Interface Sci.* **2021**, *604*, 340−349.

(60) Mohamed, S. G.; Hussain, I.; Shim, J. J. One-Step Synthesis of Hollow C-$NiCo_2S_4$ Nanostructures for High-Performance Supercapacitor Electrodes. *Nanoscale* **2018**, *10*, 6620−6628.

(61) Yao, M.; Hu, Z.; Xu, Z.; Liu, Y.; Liu, P.; Zhang, Q. High-Performance Electrode Materials of Hierarchical Mesoporous Nickel Oxide Ultrathin Nanosheets Derived from Self-Assembled Scroll-like α-Nickel Hydroxide. *J. Power Sources* **2015**, *273*, 914−922.

(62) Mohamed, S. G.; Attia, S. Y.; Hassan, H. H. Spinel-Structured $FeCo_2O_4$ Mesoporous Nanosheets as Efficient Electrode for Supercapacitor Applications. *Microporous Mesoporous Mater.* **2017**, *251*, 26−33.

(63) Hu, H.; Guan, B. Y.; Lou, X. W. (David). Construction of Complex CoS Hollow Structures with Enhanced Electrochemical Properties for Hybrid Supercapacitors. *Chem* **2016**, *1*, 102−113.

(64) Liu, X.; Ma, C.; Wen, Y.; Chen, X.; Zhao, X.; Tang, T.; Holze, R.; Mijowska, E. Highly Efficient Conversion of Waste Plastic into Thin Carbon Nanosheets for Superior Capacitive Energy Storage. *Carbon* **2021**, *171*, 819−828.

(65) Chen, X.; Hou, Y.; Wang, H.; Cao, Y.; He, J. Facile Deposition of Pd Nanoparticles on Carbon Nanotube Microparticles and Their Catalytic Activity for Suzuki Coupling Reactions. *J. Phys. Chem. C* **2008**, *112*, 8172−8176.

(66) Chen, X.; Kierzek, K.; Cendrowski, K.; Pelech, I.; Zhao, X.; Feng, J.; Kalenczuk, R. J.; Tang, T.; Mijowska, E. CVD Generated Mesoporous Hollow Carbon Spheres as Supercapacitors. *Colloids Surf., A* **2012**, *396*, 246−250.

(67) Nguyen, T. T.; Balamurugan, J.; Aravindan, V.; Kim, N. H.; Lee, J. H. Boosting the Energy Density of Flexible Solid-State Supercapacitors via Both Ternary NiV_2Se_4 and $NiFe_2Se_4$ Nanosheet Arrays. *Chem. Mater.* **2019**, *31*, 4490−4504.

(68) Wang, Q.; Gao, F.; Xu, B.; Cai, F.; Zhan, F.; Gao, F.; Wang, Q. ZIF-67 Derived Amorphous $CoNi_2S_4$ Nanocages with Nanosheet Arrays on the Shell for a High-Performance Asymmetric Supercapacitor. *Chem. Eng. J.* **2017**, *327*, 387−396.

(69) Zardkhoshoui, A. M.; Davarani, S. S. H. Construction of Complex Copper-Cobalt Selenide Hollow Structures as an Attractive Battery-Type Electrode Material for Hybrid Supercapacitors. *Chem. Eng. J.* **2020**, *402*, 126241−126252.

(70) Mohammadi Zardkhoshoui, A.; Ameri, B.; Saeed Hosseiny Davarani, S. α-MnS@Co_3S_4 Hollow Nanospheres Assembled from Nanosheets for Hybrid Supercapacitors. *Chem. Eng. J.* **2021**, *422*, No. 129953.

(71) Guan, X.; Huang, M.; Yang, L.; Wang, G.; Guan, X. Facial Design and Synthesis of CoS_x/Ni-Co LDH Nanocages with Rhombic Dodecahedral Structure for High-Performance Asymmetric Supercapacitors. *Chem. Eng. J.* **2019**, *372*, 151−162.

(72) Li, H. B.; Yu, M. H.; Wang, F. X.; Liu, P.; Liang, Y.; Xiao, J.; Wang, C. X.; Tong, Y. X.; Yang, G. W. Amorphous Nickel Hydroxide Nanospheres with Ultrahigh Capacitance and Energy Density as Electrochemical Pseudocapacitor Materials. *Nat. Commun.* **2013**, *4*, No. 1894.

(73) Jing, M.; Hou, H.; Banks, C. E.; Yang, Y.; Zhang, Y.; Ji, X. Alternating Voltage Introduced NiCo Double Hydroxide Layered Nanoflakes for an Asymmetric Supercapacitor. *ACS Appl. Mater. Interfaces* **2015**, *7*, 22741−22744.

(74) Liu, Y.; Wang, Y.; Shi, C.; Chen, Y.; Li, D.; He, Z.; Wang, C.; Guo, L.; Ma, J. Co-ZIF Derived Porous NiCo-LDH Nanosheets/N Doped Carbon Foam for High-Performance Supercapacitor. *Carbon* **2020**, *165*, 129−138.

(75) Lu, W.; Yang, M.; Jiang, X.; Yu, Y.; Liu, X.; Xing, Y. Template-Assisted Synthesis of Hierarchically Hollow C/$NiCo_2S_4$ Nanospheres Electrode for High Performance Supercapacitors. *Chem. Eng. J.* **2020**, *382*, No. 122943.

(76) Yu, F.; Chang, Z.; Yuan, X.; Wang, F.; Zhu, Y.; Fu, L.; Chen, Y.; Wang, H.; Wu, Y.; Li, W. Ultrathin $NiCo_2S_4$@graphene with a Core-Shell Structure as a High Performance Positive Electrode for Hybrid Supercapacitors. *J. Mater. Chem. A* **2018**, *6*, 5856−5861.

(77) Fu, Y.; Song, J.; Zhu, Y.; Cao, C. High-Performance Supercapacitor Electrode Based on Amorphous Mesoporous Ni-$(OH)_2$ Nanoboxes. *J. Power Sources* **2014**, *262*, 344−348.